

Chapter 4

Wind Field Diagnostic Model

E. Rodríguez, G. Montero and A. Oliver

Abstract This chapter describes Wind3D, a mass-consistent diagnostic model with an updated vertical wind profile and atmospheric parameterization. First, a description of Wind3D is provided, along with their governing equations. Next, the finite element formulation of the model and the description of the solver of the corresponding linear system is presented. The model requires an initial wind field, interpolated from data obtained in a few points of the domain. It is constructed using a logarithmic wind profile that consider the effect of both stable boundary layer (SBL) and the convective boundary layer (CBL). One important aspect of mass-consistent models is that they are quite sensitive to the values of some of their parameters. To deal with this problem, a strategy for parameter estimation based in a memetic algorithm is presented. Finally, a numerical experiment over complex terrain is presented along with some concluding remarks.

4.1 Mass consistent model

Diagnostic models apply conservation of mass, momentum, and energy singularly or fully, considering the terrain effects on an initial flow field. Although these models are used to obtain wind fields at a given time, the results usually represent winds of a time-averaged period. Diagnostic models are limited in comparison with prognostic models because they don't take into account the transient and thermal effects so they cannot simulate the evolution of the boundary layer; however, the computational requirements of the former are much lower than the latter.

Eduardo Rodríguez · Gustavo Montero · Albert Oliver
University Institute for Intelligent Systems and Numerical Applications in Engineering, University of Las Palmas de Gran Canaria, Edificio Central del Parque Tecnológico, Campus de Tafira, 35017, Las Palmas de Gran Canaria, Spain e-mail: eduardo.rodriguez@ulpgc.es, gus-tavo.montero@ulpgc.es, albert.oliver@ulpgc.es

Diagnostic models can be classified into three different categories according to the conservation laws applied. The first category comprises the diagnostic models that are based only on the conservation of mass; see, e.g., [21, 16, 4]. These models obtain a divergence-free flow that minimizes the differences with an initial known wind field. Mass-consistent models have been applied to the dynamical-downscaling of NWP models for local and regional scale wind forecasting, e.g., the WindNinja model [25]. The second category considers a linearized momentum equation [26, 19]. Non-linear momentum effects in steep terrain are not represented by these models [11]. Compared to the mass-consistent models, computational cost is comparable providing similar results [27, 3]. Nevertheless, mass-consistent models are better suited than linearized models for some atmospheric dispersion problems where a fast response is required [10]. The third type of diagnostic model applies conservation of both mass and momentum to some form of turbulence closure [2, 12, 24, 11], and even conservation of energy [14]. The RANS RNG $k - \epsilon$ turbulence model has handled non-linear flow effects better than mass-consistent models [11] but it is computationally more expensive.

Wind3D uses the logarithmic wind profile to construct the initial wind field. Under this profile, the value of z_0 is the height above ground level where the wind speed follows the logarithmic law and below that height the wind speed is considered zero. The value of d preserves the logarithmic law above tall obstacles [6]. Both z_0 and d determines the effect of the land cover to the near-surface airflow [1]. Therefore, the values of these parameters are directly related to the vegetation and topographical characteristics of the terrain, which can be defined by the land coverage of the terrain, as explained in Chapter 2.

4.1.1 Governing equation

We consider a mass-consistent model [21, 16, 18, 7] to compute a wind field u in a domain Ω with a boundary $\Gamma = \Gamma_a \cup \Gamma_b$, which satisfies the mass continuity equation in Ω , for an incompressible flow, and the impermeability condition on the terrain Γ_a :

$$\nabla \cdot \mathbf{u} = 0 \text{ in } \Omega \quad (4.1)$$

$$\mathbf{n} \cdot \mathbf{u} = 0 \text{ in } \Gamma_a \quad (4.2)$$

where n is the outward-pointing normal unit vector and Γ_b the free boundary. The model formulates a least-squares problem in the domain Ω to find a wind field $\mathbf{u}(\tilde{u}, \tilde{v}, \tilde{w})$ such that it is adjusted as much as possible to an interpolated wind field $\mathbf{v}_0(u_0, v_0, w_0)$. The adjusting functional for a field $\mathbf{u}(\tilde{u}, \tilde{v}, \tilde{w})$ is defined as:

$$E(\tilde{u}, \tilde{v}, \tilde{w}) = \int_{\Omega} [\alpha_1^2 ((\tilde{u} - u_0)^2 + (\tilde{v} - v_0)^2) + \alpha_2^2 (\tilde{w} - w_0)^2] d\Omega \quad (4.3)$$

being α_1 and α_2 the Gauss Precision moduli, considered equal for the horizontal direction. Mass consistent models are very sensitive to the values chosen for α_1 and α_2 , so special care must be taken in its selection. Dividing equation 4.3 by α_2^2 leads to the so called stability parameter α ,

$$\alpha = \frac{\alpha_1}{\alpha_2} \quad (4.4)$$

Note that coefficients α_1 and α_2 are the adjusting weights for the horizontal and vertical components of wind velocity. For $\alpha \gg 1$ vertical wind component has more weight, so wind tends to pass over terrain barriers; with $\alpha \ll 1$ wind tends to surround such barriers. In particular, there is pure vertical adjustment for $\alpha \rightarrow \infty$, while $\alpha \rightarrow 0$ means pure horizontal adjustment.

In order to find the wind field $\mathbf{v}(u, v, w)$ the following problem must be solved:

“Find $\mathbf{v} \in K$ such that,

$$E(\mathbf{v}) = \min_{\mathbf{u} \in K} E(\mathbf{u}), \quad K = \{\mathbf{u}; \nabla \cdot \mathbf{u} = 0, \mathbf{n} \cdot \mathbf{u}|_{\Gamma_b} = 0\}” \quad (4.5)$$

This problem is equivalent to finding the saddle point (\mathbf{v}, ϕ) of Lagrangian [28],

$$L(\mathbf{u}, \lambda) = E(\mathbf{u}) + \int_{\Omega} \lambda \nabla \cdot \mathbf{u} d\Omega \quad (4.6)$$

The Lagrange multiplier technique can be used to obtain the saddle point of equation (4.6), $L(\mathbf{v}, \lambda) \leq L(\mathbf{v}, \phi) \leq L(\mathbf{u}, \phi)$, such that the solution field \mathbf{v} can be obtained from Euler-Lagrange equations,

$$\mathbf{v} = \mathbf{v}_0 + T \nabla \phi \quad (4.7)$$

being ϕ Lagrange multiplier and $T = (T_h, T_h, T_v)$ the diagonal transmissivity tensor

$$T_h = \frac{1}{2\alpha_1^2}, \quad T_v = \frac{1}{2\alpha_2^2} \quad \text{y} \quad \frac{T_v}{T_h} = \alpha^2 \quad (4.8)$$

If α_1 and α_2 are considered constant in the whole domain, variational formulation leads to an elliptic equation defined in ϕ . Substituting equation (4.7) in (4.1) results in

$$-\nabla \cdot (T \nabla \phi) = \nabla \cdot \mathbf{v}_0 \quad (4.9)$$

which can be completed with null Dirichlet condition in the permeable boundaries of the domain (vertical boundaries)

$$\phi = 0 \quad \text{in} \quad \Gamma_a \quad (4.10)$$

and a Neumann condition in the non-permeable boundaries (terrain and upper boundary)

$$\mathbf{n} \cdot T \nabla \phi = -\mathbf{n} \cdot \mathbf{v}_0 \text{ in } \Gamma_b \quad (4.11)$$

Taking into account that the initial wind field \mathbf{v}_0 is horizontal in the upper boundary, condition 4.11 becomes

$$\mathbf{n} \cdot T \nabla \phi = 0 \quad (4.12)$$

Considering T_h and T_v as constants, equation (4.9) becomes

$$\frac{\partial^2 \phi}{\partial x^2} + \frac{\partial^2 \phi}{\partial y^2} + \alpha^2 \frac{\partial^2 \phi}{\partial z^2} = -\frac{1}{T_h} \left(\frac{\partial u_0}{\partial x} + \frac{\partial v_0}{\partial y} + \frac{\partial w_0}{\partial z} \right) \quad (4.13)$$

4.1.2 Finite element formulation

The classic formulation given in equations (4.9), (4.10) and (4.11) is solved using the finite element method (FEM) and tetrahedral meshes (see Chapter 3).

Note that in the variational formulation of the problem, integrals in the boundary with Neumann condition are canceled using equation (4.11), while those corresponding to Dirichlet conditions are eliminated canceling out the corresponding test function.

This leads to a set of elemental matrices of dimension 4×4 associated to the element Ω_e , being $\hat{\psi}_i$ the shape function corresponding to the i -th node, $i = 1, 2, 3, 4$, defined in the reference element $\hat{\Omega}_e$ and $|\mathbf{J}|$ the jacobian of the transformation of Ω_e into $\hat{\Omega}_e$,

$$\begin{aligned} \{\mathbf{A}^e\}_{ij} = & \int_{\hat{\Omega}_e} \left\{ \left(\frac{\partial \hat{\psi}_i}{\partial \xi} \frac{\partial \xi}{\partial x} + \frac{\partial \hat{\psi}_i}{\partial \eta} \frac{\partial \eta}{\partial x} + \frac{\partial \hat{\psi}_i}{\partial \varphi} \frac{\partial \varphi}{\partial x} \right) \left(\frac{\partial \hat{\psi}_j}{\partial \xi} \frac{\partial \xi}{\partial x} + \frac{\partial \hat{\psi}_j}{\partial \eta} \frac{\partial \eta}{\partial x} + \frac{\partial \hat{\psi}_j}{\partial \varphi} \frac{\partial \varphi}{\partial x} \right) \right. \\ & + \left(\frac{\partial \hat{\psi}_i}{\partial \xi} \frac{\partial \xi}{\partial y} + \frac{\partial \hat{\psi}_i}{\partial \eta} \frac{\partial \eta}{\partial y} + \frac{\partial \hat{\psi}_i}{\partial \varphi} \frac{\partial \varphi}{\partial y} \right) \left(\frac{\partial \hat{\psi}_j}{\partial \xi} \frac{\partial \xi}{\partial y} + \frac{\partial \hat{\psi}_j}{\partial \eta} \frac{\partial \eta}{\partial y} + \frac{\partial \hat{\psi}_j}{\partial \varphi} \frac{\partial \varphi}{\partial y} \right) + \\ & \left. + \frac{T_v}{T_h} \left(\frac{\partial \hat{\psi}_i}{\partial \xi} \frac{\partial \xi}{\partial z} + \frac{\partial \hat{\psi}_i}{\partial \eta} \frac{\partial \eta}{\partial z} + \frac{\partial \hat{\psi}_i}{\partial \varphi} \frac{\partial \varphi}{\partial z} \right) \left(\frac{\partial \hat{\psi}_j}{\partial \xi} \frac{\partial \xi}{\partial z} + \frac{\partial \hat{\psi}_j}{\partial \eta} \frac{\partial \eta}{\partial z} + \frac{\partial \hat{\psi}_j}{\partial \varphi} \frac{\partial \varphi}{\partial z} \right) \right\} \cdot |\mathbf{J}| \, d\xi \, d\eta \, d\varphi \end{aligned} \quad (4.14)$$

and elemental vectors of dimension 4×1 ,

$$\begin{aligned} \{\mathbf{b}^e\}_i = & \int_{\hat{\Omega}_e} -\frac{1}{T_h} \left\{ u_0 \left(\frac{\partial \hat{\psi}_i}{\partial \xi} \frac{\partial \xi}{\partial x} + \frac{\partial \hat{\psi}_i}{\partial \eta} \frac{\partial \eta}{\partial x} + \frac{\partial \hat{\psi}_i}{\partial \varphi} \frac{\partial \varphi}{\partial x} \right) + \right. \\ & + v_0 \left(\frac{\partial \hat{\psi}_i}{\partial \xi} \frac{\partial \xi}{\partial y} + \frac{\partial \hat{\psi}_i}{\partial \eta} \frac{\partial \eta}{\partial y} + \frac{\partial \hat{\psi}_i}{\partial \varphi} \frac{\partial \varphi}{\partial y} \right) + \\ & \left. + w_0 \left(\frac{\partial \hat{\psi}_i}{\partial \xi} \frac{\partial \xi}{\partial z} + \frac{\partial \hat{\psi}_i}{\partial \eta} \frac{\partial \eta}{\partial z} + \frac{\partial \hat{\psi}_i}{\partial \varphi} \frac{\partial \varphi}{\partial z} \right) \right\} \cdot |\mathbf{J}| \, d\xi \, d\eta \, d\varphi \end{aligned} \quad (4.15)$$

4.1.3 Linear system resolution

The application of finite element method to these problems leads to the resolution of large and symmetric linear systems of equations with a sparse matrix of coefficients (stiffness matrix):

$$\mathbf{Ax} = \mathbf{b} \quad (4.16)$$

Using iterative solvers is an appropriate strategy to solve such linear systems. In particular, the conjugated gradient method [9] is the most efficient Krylov's subspace method for solving symmetric linear systems.

In the case of a sparse matrix, major memory requirement reductions can be achieved by storing only the non-zero entries in the computer memory. In particular, the compressed storage row technique uses three one-dimensional arrays to represent the stiffness matrix, that respectively contain nonzero values, the extents of rows and column indices. An storage of order $3 \times n$ (being n the matrix dimension) is needed, in contrast to n^2 needed for the whole representation (including zero coefficients). The trade-off is that accessing the individual elements becomes more complex and additional structures are needed to be able to recover the original matrix unambiguously.

The solution, ϕ , of the linear system is used to obtain the wind field with equation 4.7.

The rate of convergence of methods based on Krylov subspaces, and conjugated gradient in particular, can be improved with the use of preconditioning techniques. In general, they consist of replacing the original system of equations (4.16) by another one with identical solution, in such a way that the condition of the matrix of the new system is lower than that of \mathbf{A} . In general, a preconditioning matrix \mathbf{M}^{-1} is considered, being \mathbf{M} an approximation of \mathbf{A} ,

$$\mathbf{M}^{-1}\mathbf{Ax} = \mathbf{M}^{-1}\mathbf{b} \quad (4.17)$$

such that, $\kappa(\mathbf{M}^{-1}\mathbf{A}) < \kappa(\mathbf{A})$.

The lowest value corresponds to ideal case $\mathbf{M} = \mathbf{A}$, $\kappa(\mathbf{A}^{-1}\mathbf{A}) = 1$, with the system converging in one iteration, but the computational cost of obtaining \mathbf{A}^{-1} would be equivalent to solve the system by means of a direct method. The objective is to calculate a matrix \mathbf{M} as close to \mathbf{A} as possible with low computational cost.

Matrix \mathbf{M} should also be easily invertible in order to have a reasonable computational cost in \mathbf{M}^{-1} -vector products in the preconditioned algorithms.

The preconditioning may be carried out in three different ways,

$$\begin{aligned} \mathbf{M}^{-1}\mathbf{Ax} &= \mathbf{M}^{-1}\mathbf{b} && \text{(Left preconditioning)} \\ \mathbf{AM}^{-1}\mathbf{Mx} &= \mathbf{b} && \text{(Right preconditioning)} \\ \mathbf{M}_1^{-1}\mathbf{AM}_2^{-1}\mathbf{M}_2\mathbf{x} &= \mathbf{M}_1^{-1}\mathbf{b} && \text{(Both sides preconditioning)} \end{aligned} \quad (4.18)$$

if \mathbf{M} can be factorized as $\mathbf{M} = \mathbf{M}_1\mathbf{M}_2$. Preconditioned Conjugated Gradient method is shown in algorithm 2.

A number of preconditioners have been developed and widely used in several application fields; see, e.g., [15]. Despite we have achieved good results in our simulations with Wind3D using the Jacobi preconditioner, i.e., $\mathbf{M} = \text{diag}(\mathbf{A})$, in [23] can be found a specific preconditioner for this wind problem.

Algorithm 2 Preconditioned Conjugate Gradient (PCG).

```

1: Initial approximation  $\mathbf{x}_0$ .  $\mathbf{r}_0 = \mathbf{b} - \mathbf{A}\mathbf{x}_0$ ;
2: Solve  $\mathbf{M}\mathbf{z}_0 = \mathbf{r}_0$ ,  $\mathbf{p}_0 = \mathbf{z}_0$ ;
3: while  $\|\mathbf{r}_j\| / \|\mathbf{r}_0\| \geq \varepsilon$  ( $j = 0, 1, 2, 3, \dots$ ) do
4:    $\alpha_j = \frac{\langle \mathbf{r}_j, \mathbf{z}_j \rangle}{\langle \mathbf{A}\mathbf{p}_j, \mathbf{p}_j \rangle}$ ;
5:    $\mathbf{x}_{j+1} = \mathbf{x}_j + \alpha_j \mathbf{p}_j$ ;
6:    $\mathbf{r}_{j+1} = \mathbf{r}_j - \alpha_j \mathbf{A}\mathbf{p}_j$ ;
7:   Solve  $\mathbf{M}\mathbf{z}_{j+1} = \mathbf{r}_{j+1}$ ;
8:    $\beta_j = \frac{\langle \mathbf{r}_{j+1}, \mathbf{z}_{j+1} \rangle}{\langle \mathbf{r}_j, \mathbf{z}_j \rangle}$ ;
9:    $\mathbf{p}_{j+1} = \mathbf{z}_{j+1} + \beta_j \mathbf{p}_j$ ;
10: end while

```

4.1.4 Construction of the interpolated wind field

The first step of Wind3D is to create an initial wind field using wind data available only in a few locations on the domain. Data is typically obtained from wind measurement stations or from large scale numerical weather models with coarse grids. With this data, a suitable interpolation is performed in order to construct a wind field on the whole domain, using a logarithmic vertical profile.

At this stage, we want to interpolate the available wind data at any point located at a height z_m over $z_t + d$, where z_t is the terrain surface height. If we have a set of dispersed data, a simple technique for this interpolation is formulated as a weighted sum of the inverse-square law and the height difference interpolation [16]:

$$u_0(z_m) = \xi \frac{\sum_{i=1}^{n_h} \frac{u_i^h}{\delta_i^2}}{\sum_{i=1}^{n_h} \frac{1}{\delta_i^2}} + (1 - \xi) \frac{\sum_{i=1}^{n_h} \frac{u_i^h}{|\Delta h_i|}}{\sum_{i=1}^{n_h} \frac{1}{|\Delta h_i|}}, \quad (4.19)$$

where the value of u_i^h is the wind velocity at the point i ; n_h is the number of available points; δ_i is the horizontal distance between point i and the point of interest; $|\Delta h_i|$ is their height difference, and ξ is a weighting parameter ($0 \leq \xi \leq 1$) that determines to what degree the focus is put on the inverse-square law or the height difference interpolation.

When a grid of wind data is available, e.g., downscaling HARMONIE-AROME or ECMWF wind results, it is preferable to interpolate the wind field with a simple bilinear Lagrange interpolation in the cell containing the studied point.

The next step is the construction of the vertical wind profile. We have implemented the log wind profile proposed in [30] for stable/neutral conditions (see Chapter 2):

$$u = \frac{u_*}{k} \left(\ln \frac{\zeta}{\zeta_0} + b_1 (\zeta - \zeta_0) + b_2 (\zeta - \zeta_0)^2 + b_3 (\zeta - \zeta_0)^3 \right), \quad (4.20a)$$

$$v = -\frac{u_*}{k} \delta \left(-(\zeta - \zeta_0) \ln(\zeta - \zeta_0) + a_1 (\zeta - \zeta_0) + a_2 (\zeta - \zeta_0)^2 + a_3 (\zeta - \zeta_0)^3 \right), \quad (4.20b)$$

for $z > d + z_0$, where u and v are the components of the horizontal wind velocity along the x and y axis of a right-hand Cartesian coordinate system with the x -axis along the surface stress; $\zeta = (z - d)/h$ and $\zeta_0 = z_0/h$ are dimensionless heights; $k \approx 0.4$ is the von Kármán constant; $\delta = fh/(ku_*) = \gamma/k$ is the dimensionless rotation rate parameter; $a_1 = 4/\delta^2 + \bar{\Pi}$, $a_2 = -\frac{3}{2}\bar{\Pi}$, $a_3 = \frac{1}{3}(1 - 4/\delta^2 + 2\bar{\Pi})$, $b_1 = \bar{\Pi} - 3$, $b_2 = -\frac{3}{2}\bar{\Pi}$, $b_3 = \frac{2}{3}(\bar{\Pi} + 1)$, with $\bar{\Pi} = C_R \delta^2 + C_L \frac{kh}{L} + C_N \frac{Nh}{u_*}$ and $\bar{\Pi} = \bar{C}_R \delta^2 + \bar{C}_L \frac{kh}{L} + \bar{C}_N \frac{Nh}{u_*}$; and $L = -u_*^3/(kB_s)$ is the Monin-Obukhov length. This model uses the values of estimates of the dimensionless constants obtained by [30] on the basis of empirical and numerical (LES) data: $C_R = 7$, $C_L = 4.5$, $C_N = 0.4$, $\bar{C}_R = 0$, $\bar{C}_L = -7$, $\bar{C}_N = -1$. In addition, the original expression in [30] has been slightly modified to verify $u(z) = 0$ and $v(z) = 0$ at $z = d + z_0$. The vertical component w of the wind velocity is assumed to be zero. From (4.20a), the surface friction velocity may be computed using the horizontal wind velocity interpolated at $z = z_m$, $u_0(z_m)$:

$$\ln \frac{z_m - d}{z_0} u_*^3 - \left[ku_0(z_m) - \left(C_R \frac{\gamma}{k^2} + \frac{C_N N_{2h-h}}{f} - \frac{3}{\gamma} \right) f(z_m - (d + z_0)) \right] u_*^2 - C_L k^2 B_s(z_m - (d + z_0)) = 0 \quad (4.21)$$

where the squared and cubic terms of the wind profile were neglected at $z = z_m$.

The estimation of the CBL height is provided by the mesoscale model estimations (see Chapter 2). If the ratio between the mechanical velocity scale $V_* = (2Uu_*)^{1/3}$ and the convective velocity scale $W_* = (B_s h)^{1/3}$ is negligible, i.e., $V_*/W_* \ll 1$, we have a Purely Convective Layer (PCL). Otherwise, it is a Mechanically-Convective Layer (MCL) [31]. The log wind profile in the CBL was given in [29] as follows:

$$|u| = \begin{cases} \frac{u_*}{k} \ln \frac{z-d}{z_0} & z_0 + d < z < \frac{\zeta_u |L|}{k} + d, \quad (4.22a) \\ \frac{u_*}{k} \left[a_u + C_u \left(\frac{k(z-d)}{L} \right)^{-\frac{1}{3}} + \ln \frac{-L}{kz_0} \right] & \frac{\zeta_u |L|}{k} + d \leq z \leq h, \quad (4.22b) \end{cases}$$

where $\zeta_u \approx 0.1$, $a_u \approx 0.7$ and $C_u \approx 1.4$ are dimensionless constants (see [4]). The angle of wind turn in the boundary layer is given by the expression:

$$\sin \alpha = \sin(\alpha_s - \alpha_{h-0}) = \frac{a_\alpha}{k} \left(\frac{hk}{|L|} \right)^{-\frac{1}{3}} \frac{u_*}{|\bar{u}|} \operatorname{sign} f, \quad (4.23)$$

where α_s and α_{h-0} are the angles between the wind direction and x -axis at the terrain and $z = h$, respectively. The estimation of $a_\alpha = 3$ was proposed in [29]. The mean wind velocity $|\bar{u}|$ in the CBL is obtained from:

$$|\bar{u}| = |u|_{h-0} = \frac{u_*}{k} \left[a_u + \ln \frac{-L}{kz_0} \right], \quad (4.24)$$

if we consider $h \gg |L|$. In practice, we assume that the wind turn angle varies linearly with height and reaches zero at the top of the CBL. Finally, note that in the CBL wind profile, the calculation of the surface friction velocity u_* from the horizontal wind velocity interpolated at $z = z_m$, $u_0(z_m)$, is generally straightforward using (4.22a):

$$u_* = \frac{k |u_0(z_m)|}{\ln \frac{z_m - d}{z_0}}. \quad (4.25)$$

In the case that $z_m \geq \frac{\zeta_u |L|}{k} + d$, we have to use (4.22b).

4.2 Parameter estimation

The results of the mass-consistent modeling have proved to be very sensitive to the values of α , ξ , z_0 , and d . Thus, an accurate definition of these parameters is critical to obtain a reliable downscaling wind field. We have to estimate a value of α and ξ for the whole domain [18], and a value of z_0 and d for each land cover class. This means that the number of unknowns depends on the number of the different land covers in the region of interest.

The objective of the optimization is to find the values of the parameters such that the wind computed with the model is the most similar to a known wind at some control points. The wind values at the control points can be known from a NWP model (i.e. HARMONIE-AROME) or from measurement stations. To measure the error between the model and the known data, we use the RMSE, i.e.,

$$RMSE = \sqrt{\frac{1}{n_c} \sum_{i=1}^{n_c} (u_{xi} - u_{xi}^c)^2 + (u_{yi} - u_{yi}^c)^2 + (u_{zi} - u_{zi}^c)^2}, \quad (4.26)$$

where n_c is the number of control points, (u_{xi}, u_{yi}, u_{zi}) and $(u_{xi}^c, u_{yi}^c, u_{zi}^c)$ are, respectively, the wind velocity obtained with the mass-consistent model and the known wind at the i^{th} control point. So, the parameter estimation consists of the minimization of the RMSE. Note that for each evaluation of the fitness function, the wind model has to be executed.

Evolutionary algorithms are a family of heuristic optimization methods using techniques inspired in biology to find out optimal configuration for a specific system within given constraints. For this reason they can be used to estimate the parameters stated above. We have successfully used a classic genetic algorithm [17, 20] algorithm to estimate parameters of a simplified version of Wind3D that does not consider any land cover parameters. In the next section we present a memetic algorithm to optimize the fitness function (4.26).

Note that the values of z_0 and d obtained in a particular numerical experiment are not representative values for a given land cover; they only represent the optimal solution compared to the available wind measurements for the land covers in the domain of interest. However, the general methodology can be applied to any combination of regions, databases, and downscaling wind models. So, the final aim of the proposed strategy is to improve the results of a downscaling wind model by estimating the optimum aerodynamic parameters values.

4.2.1 Memetic Algorithm

As stated before, an evolutionary algorithm is a suitable technique to find the optimal values of the parameters of the wind field model. A population of individual representing different values of the parameters is allowed to evolve during a number of iterations (generations). In each one, the selected individuals, according to the fitness function, are combined to create the next population. During the process, some of the individuals can go under mutation. Finally, the fittest individual is chosen as solution of the optimization problem.

The generic denomination of Memetic Algorithms (MAs) is used to encompass a broad class of metaheuristics (i.e. general purpose methods aimed to guide an underlying heuristic). In this case, we propose a memetic method composed of three tools: the differential evolution algorithm (DE) [22], a Rebirth Operator (RBO) [8], and the L-BFGS-B algorithm [5]. DE is an evolutionary algorithm that utilizes a population composed of a fixed number n_v of D -dimensional parameter vectors $p_{i,g}$ for each generation g ; $g = 1, \dots, n_g$. The initial population, which must cover the parameter searching space, is chosen randomly. The mutation procedure modifies an existing vector by adding to itself a weighted difference between two other vectors. In the crossover step, these mutated vectors are mixed with another target vector to obtain the so-called trial vector. If the trial vector yields a lower fitness function value than the target vector, the target vector is replaced by the trial vector (selection). Each population vector has to serve as target vector at least once, so n_v competitions will take place per generation.

The accuracy of the results obtained using DE may be insufficient. To increase it, we have run n_e DE experiments and have performed a statistic analysis of the results obtained for each one. This analysis will allow us to reduce the search interval. Let p_{i,n_g}^j ($j = 1, \dots, n_e$; $i = 1, \dots, n_u$) be the estimation of the n_u unknown parameters obtained in each of the n_e experiments. We can compute its average \bar{p}_{i,n_g} , and standard

deviation σ_{i,n_g} . Then, the search interval can be reduced to the confidence interval of each variable, i.e., $\bar{p}_{i,n_g} \pm \frac{\sigma_{i,n_g}}{\sqrt{n_e}} T_{n_e-1, \frac{\tau}{2}}$, where $1 - \tau$ is the confidence coefficient and T , the Student's t-distribution. If one extreme of the new interval exceeds the old extreme, the latter is preserved. This allows the rebirth of a new population to restart DE. This procedure may be repeated as many times as required. Note that the n_e DE experiments can be run in parallel.

When the last generation of the last reborn population is evaluated, the best parameter vector among all the DE experiments is selected to be the starting point of the L-BFGS-B algorithm. This algorithm is a procedure for solving large non-linear optimization problems with simple bounds. It is based on the gradient projection method and uses a limited memory BFGS matrix to approximate the Hessian of the fitness function. The results of this final minimization will be the estimated parameters.

4.3 Numerical experiment

In this section we characterize the roughness length and displacement height in the island of Gran Canaria (N27°58' W15°36'), Spain. To this end, a map of z_0 and d is constructed. Many authors have concluded that the roughness length and height displacement values depend on the wind speed and direction, as well as on the atmospheric stability class. Therefore, the characterization is performed for different typical meteorological episodes. For this reason, we have studied the characteristics of the wind in Gran Canaria for the summer months of 2015, i.e., from June to September.

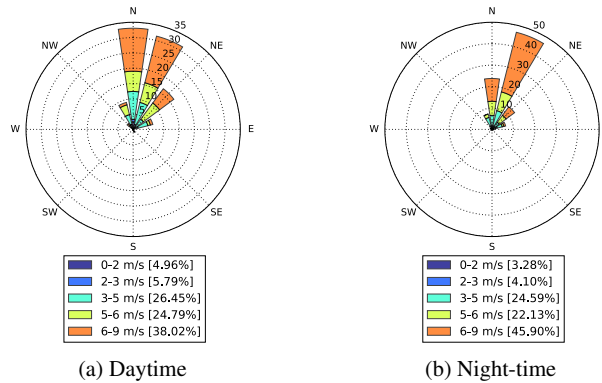


Fig. 4.1: Wind Rose of Gran Canaria at 10m relating to the period from June 1 to September 30 of the year 2015.

Figure 4.1 represents the wind roses of Gran Canaria in the selected months. For convenience, we have separated daytime and night-time. Based on this classification in speeds and directions, we have selected eight characteristic winds that represent about 71.90% of daytime and 77.88% of night-time.

Table 4.1: Most frequent wind speeds and directions in the island of Gran Canaria during the summer months.

Cases		Daytime			
Surface wind direction	Surface wind speed range (m/s)	AROME/HARMONIE 10 m wind speed	AROME/HARMONIE 10 m wind direction	Incoming solar radiation	Pasquill stability class
NNE	> 6	7.61	32.89	530.85	D
NE	> 6	9.01	37.29	583.39	D
N	> 6	7.11	349.53	494.75	D
NE	5 – 6	5.57	40.50	665.60	C
N	3 – 5	4.16	4.26	797.14	B
NNE	5 – 6	5.88	12.76	771.82	C
NNE	3 – 5	3.54	12.70	586.43	C
N	5 – 6	5.39	350.28	695.26	C

Cases		Night-time			
Surface wind direction	Surface wind speed range (m/s)	AROME/HARMONIE 10 m wind speed	AROME/HARMONIE 10 m wind direction	Cloud amount (oktas)	Pasquill stability class
NNE	> 6	9.87	25.75	4.59	D
NE	> 6	8.07	34.16	3.39	D
N	> 6	6.82	355.35	7.04	D
NE	5 – 6	5.10	42.58	2.24	D
N	3 – 5	4.99	359.27	6.45	D
NNE	5 – 6	5.13	19.94	0.61	D
NNE	3 – 5	4.90	12.56	0.00	E
N	5 – 6	5.62	353.72	1.86	D

Table 4.1 displays the chosen episodes. The AROME/HARMONIE forecast wind speeds and directions are taken at a representative point located in the sea in the NE of the island with a height of 10m above the sea. The Pasquill stability class has been obtained from the daytime incoming solar radiation and the night-time cloud amount [13].

So, we are going to estimate the parameters α , ξ , as well as z_0 and d for each of the 30 basic land covers of Gran Canaria for each of the eight episodes. The land use of Gran Canaria is obtained from the SIOSE database. According to it, in the island there are 5237 different zones with its particular linear combinations of these 30 basic classes; see Figure 4.2.

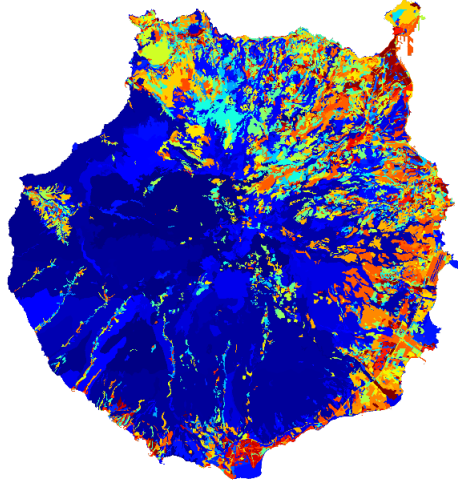


Fig. 4.2: SIOSE land cover polygons in the Island of Gran Canaria.

Table 4.2: Location in UTM zone 28N coordinates and height above the sea level of the anemometers used in the numerical application in Gran Canaria.

Code	Name	$x(m)$	$y(m)$	$z(m)$
C619X	Agaete	429982	3108624	15
C629Q	Mogán, Puerto Rico	429927	3073056	20
C648N	Telde, Centro Forestal Doramas	454970	3095890	354
C649R	Telde, Melenara	462854	3095804	19
C656V	Teror	446227	3105674	693
C659M	Plaza de la Feria	458627	3109809	25
C669B	Arucas	450225	3113015	96
C689E	Maspalomas	441057	3068075	35

In addition, wind measures at 7 stations of the State Meteorological Agency of Spain (AEMET) network are available. Its UTM coordinates and heights above sea level are given in Tab. 4.2 and shown in Fig. 4.3.

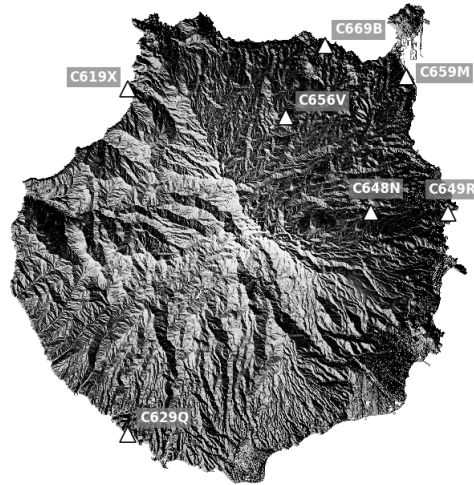


Fig. 4.3: Location of the wind measurement stations.

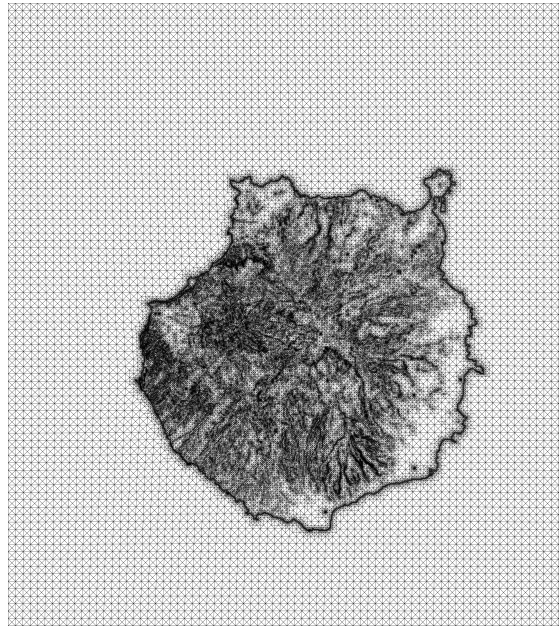


Fig. 4.4: Detail of the terrain of the adaptive mesh of Gran Canaria island.

The application is solved in a region of $76 \times 85 \text{ km}^2$ that contains the island of Gran Canaria and is limited by an upper plane at a height of 4 km . We have generated a tetrahedral mesh adapted to the terrain with local refinement around the measurement stations and the shoreline; see a detail of the terrain triangulation in Figure 4.4. The mesh contains 1492804 tetrahedra and 326101 nodes. To compute the interpolated wind field we have used the AROME/HARMONIE predictions of wind velocities at 10 m above the terrain. Finally, we have estimated the parameters using the memetic method described in section 4.2.1. We have chosen 11 control points: the measurements from the seven station and four AROME/HARMONIE wind forecast values located at 10 m over the sea in the corners of the mesh. Remember that for each evaluation of the fitness function (RMSE) the mass-consistent model has to be applied.

The results obtained for each wind episode are presented in Tab. 4.3 and 4.4 for daytime and night-time, respectively. In all of the eight episodes, using the estimated parameters, the wind predicted by the mass-consistent model has reduced the AROME/HARMONIE error. This reduction has gone from 4.97% to 56.21% in the daytime, and from 22.49% to 58.93% in the night-time. However, this approach is strongly dependent on the forecast values of the mesoscale model, which determines the quality of the predicted wind.

The literature points to a relationship between these parameters and the atmospheric state (wind speed, direction, and its stability). However, from the results presented here it is difficult to obtain a correlation between them. Particular conclusions may be drawn for some specific parameters. For example, z_0^{ARR} decreases when the wind direction goes from N to NE. Another outcome is that the range of variation of many of the parameters is considerably shorter than that given in Tab. 2.1. This is the case, e.g., for the values of z_0 corresponding to HMA, HSM, LAA, LVI, SNE and ZQM, and d in CNF, HMA, HSM, LFC, LFN, LOC, LVI, MTR, PST, RMB, SDN, SNE, ZEV and ZQM. What is clear from these experiments is that the optimal values of z_0 and d are different from the nominal values found in the literature. So, it is convenient to correct them for the region of the Canary Islands.

Concerning the values of α , there is not a direct conclusion from the results. It seems that α is normally lower at night-time than daytime, where it is more irregular, but further experiments should be carried out. Regarding ξ , it often reached values near 1.

Another important aspect to be considered is a sensibility study of all the involved parameters in the resulting wind field. This analysis may lead to a reduction of the number of unknowns by not considering those parameters with a negligible effect on the final result. One of the limitations of this approach is that one basic coverage may affect different regions with very different characteristics. However, in the current implementation each parameter is represented by a single value, but their optimal values could be different in each region. For this reason, if the sensibility analysis determines that the results of the model are highly dependent on those parameters, one can split them and consider different unknowns for each region.

Finally, this methodology can be applied to construct a reduced basis for its use in wind forecasting, but a larger period must be studied (at least one year) so that

Table 4.3: Results of the daytime experiments in Gran Canaria (z_0 and d in m).

Wind direction Wind speed (ms^{-1}) Pasquill stability	N	NNE	NE	N	NNE	NE	N	NNE
	$v > 6$	$v > 6$	$v > 6$	$5 < v \leq 6$	$5 < v \leq 6$	$5 < v \leq 6$	$3 < v \leq 5$	$3 < v \leq 5$
	D	D	D	C	C	C	B	C
<i>RMSE(AROME/HARMONIE)</i>	2.19	2.31	2.81	1.58	1.81	1.81	1.05	1.78
<i>RMSE(Wind3D)</i>	1.25	1.21	2.11	1.30	1.08	0.79	0.81	1.70
α	9.98	0.34	0.19	0.72	0.28	0.35	0.48	9.84
ξ	0.99	0.99	0.92	0.99	0.63	0.99	0.83	0.98
z_0^{ACM}	0.15	0.07	0.09	0.07	0.14	0.08	0.05	0.11
z_0^{AEM}	0.00	0.00	0.00	0.00	0.00	0.00	0.00	0.00
z_0^{ALC}	0.00	0.00	0.00	0.00	0.00	0.00	0.00	0.00
z_0^{ALG}	0.00	0.00	0.00	0.00	0.00	0.00	0.00	0.00
z_0^{AMO}	0.02	0.00	0.00	0.02	0.01	0.00	0.02	0.02
z_0^{ARR}	0.04	0.00	0.00	0.17	0.16	0.06	0.17	0.14
z_0^{CLC}	0.00	0.02	0.02	0.01	0.04	0.06	0.02	0.04
z_0^{CNF}	1.03	0.31	0.54	1.64	0.32	0.30	1.85	1.44
z_0^{CHL}	0.69	0.01	0.19	0.21	0.01	0.07	0.07	0.28
z_0^{EDF}	3.69	0.70	0.74	0.71	3.69	3.68	0.70	1.39
z_0^{FDC}	0.75	1.35	1.09	0.32	0.54	1.15	0.99	0.20
z_0^{FDP}	1.64	2.60	2.64	1.84	1.85	2.59	1.10	0.64
z_0^{HMA}	0.04	0.05	0.05	0.01	0.04	0.04	0.10	0.07
z_0^{HSM}	0.02	0.02	0.02	0.02	0.02	0.02	0.01	0.03
z_0^{LAA}	0.00	0.00	0.00	0.00	0.00	0.00	0.00	0.00
z_0^{LFC}	0.35	0.03	0.03	0.13	0.30	0.03	0.03	0.07
z_0^{LFN}	0.92	0.89	0.17	0.11	0.94	0.90	0.07	0.09
z_0^{LOC}	0.06	0.07	0.07	0.03	0.06	0.06	0.04	0.07
z_0^{LVI}	0.27	0.40	0.33	0.36	0.38	0.23	0.33	0.38
z_0^{MTR}	0.01	0.34	0.01	0.01	0.99	0.99	0.01	0.01
z_0^{OCT}	0.06	0.86	0.47	0.08	0.57	0.30	0.20	0.06
z_0^{PDA}	0.03	0.00	0.01	0.03	0.02	0.03	0.00	0.03
z_0^{PST}	0.07	0.13	0.13	0.08	0.00	0.05	0.12	0.13
z_0^{RMB}	0.00	0.00	0.00	0.00	0.00	0.00	0.00	0.00
z_0^{SDN}	0.03	0.00	0.00	0.01	0.01	0.01	0.03	0.00
z_0^{SNE}	0.02	0.00	0.01	0.01	0.03	0.00	0.00	0.02
z_0^{VAP}	0.00	0.08	0.28	0.05	0.00	0.37	0.00	0.10
z_0^{ZAU}	0.03	1.12	0.71	0.04	0.03	1.22	0.04	0.04
z_0^{ZEV}	0.14	0.00	0.00	0.00	0.15	0.13	0.09	0.08
z_0^{ZQM}	0.55	0.39	0.79	0.44	0.44	0.73	0.86	0.81
d^{ACM}	37.5	14.5	56.8	16.0	6.68	76.2	36.6	7.91
d^{ARR}	0.38	0.53	0.80	0.45	0.53	0.54	0.48	0.18
d^{CLC}	0.21	0.09	0.17	0.19	0.12	0.32	0.23	0.24
d^{CNF}	10.4	12.0	17.8	7.43	12.8	12.8	8.89	8.83
d^{CHL}	2.71	2.03	0.75	0.23	2.51	2.41	1.00	0.94
d^{EDF}	17.2	17.4	15.4	16.5	7.05	10.7	7.15	19.6
d^{FDC}	18.3	8.68	14.7	16.1	6.81	19.5	12.3	16.5
d^{FDP}	14.6	24.6	3.99	24.3	29.2	30.4	9.20	10.8
d^{HMA}	0.63	0.46	0.45	0.55	0.62	0.45	0.60	0.52
d^{HSM}	0.11	0.12	0.04	0.03	0.11	0.10	0.03	0.13
d^{LFC}	3.79	0.04	1.17	1.45	3.87	3.32	1.04	3.75
d^{LFN}	1.64	3.60	1.06	1.93	2.77	3.24	1.42	2.69
d^{LOC}	0.31	0.39	0.30	0.44	0.27	0.28	0.31	0.32
d^{LVI}	0.81	1.18	0.70	1.06	0.71	0.51	1.06	1.18
d^{MTR}	6.94	5.26	5.88	2.46	1.13	4.51	1.35	6.61
d^{OCT}	2.34	4.91	3.09	2.43	12.8	11.2	3.52	2.21
d^{PDA}	0.18	0.15	0.14	0.16	0.21	0.06	0.09	0.31
d^{PST}	0.25	0.60	0.07	0.30	0.33	0.60	0.49	0.57
d^{RMB}	0.00	0.00	0.01	0.01	0.01	0.00	0.02	0.01
d^{SDN}	0.16	0.11	0.07	0.09	0.11	0.12	0.17	0.13
d^{SNE}	0.12	0.06	0.08	0.12	0.16	0.15	0.03	0.15
d^{VAP}	2.24	1.71	1.76	0.54	0.15	1.51	0.53	0.07
d^{ZAU}	13.3	10.8	12.5	13.8	11.6	4.05	11.5	13.7
d^{ZEV}	0.16	0.37	0.22	0.16	0.25	0.69	0.23	0.33
d^{ZQM}	2.69	5.35	3.79	4.23	4.41	3.95	1.42	4.58

Table 4.4: Results of the night-time experiments in Gran Canaria (z_0 and d in m).

Wind direction Wind speed (ms^{-1}) Pasquill stability	N	NNE	NE	N	NNE	NE	N	NNE
	$v > 6$	$v > 6$	$v > 6$	$5 < v \leq 6$	$5 < v \leq 6$	$5 < v \leq 6$	$3 < v \leq 5$	$3 < v \leq 5$
	D	D	D	D	D	D	D	E
<i>RMSE(AROME/HARMONIE)</i>	3.47	3.92	3.03	2.53	2.23	1.54	2.19	2.79
<i>RMSE(Wind3D)</i>	1.47	1.61	1.34	1.28	1.73	1.10	1.19	1.43
α	0.10	0.10	0.10	0.10	9.48	0.10	0.22	0.10
ξ	0.90	0.33	0.65	0.99	0.99	0.99	0.99	0.99
z_0^{ACM}	0.10	0.11	0.06	0.10	0.17	0.13	0.11	0.07
z_0^{AEM}	0.00	0.00	0.00	0.00	0.00	0.00	0.00	0.00
z_0^{ALC}	0.00	0.00	0.00	0.00	0.00	0.00	0.00	0.00
z_0^{ALG}	0.00	0.00	0.00	0.00	0.00	0.00	0.00	0.00
z_0^{AMO}	0.00	0.02	0.02	0.00	0.00	0.00	0.00	0.01
z_0^{ARR}	0.11	0.02	0.00	0.15	0.02	0.01	0.16	0.03
z_0^{CLC}	0.04	0.04	0.01	0.02	0.05	0.03	0.05	0.03
z_0^{CNF}	0.73	0.25	0.29	0.36	1.35	0.60	0.33	0.30
z_0^{CHL}	0.13	0.00	0.36	0.57	0.70	0.71	0.19	0.01
z_0^{EDF}	1.52	0.77	0.71	2.70	2.82	0.70	3.06	0.71
z_0^{FDC}	0.67	1.25	1.24	1.24	0.23	1.15	0.53	1.24
z_0^{FDP}	2.08	2.57	2.49	0.90	0.69	2.62	0.63	2.61
z_0^{HMA}	0.03	0.10	0.05	0.07	0.11	0.09	0.11	0.12
z_0^{HSM}	0.00	0.01	0.02	0.03	0.01	0.01	0.01	0.02
z_0^{LAA}	0.00	0.00	0.00	0.00	0.00	0.00	0.00	0.00
z_0^{LFC}	0.05	0.03	0.03	0.35	0.17	0.13	0.38	0.03
z_0^{LFN}	0.07	0.06	0.07	0.44	0.07	0.24	0.10	0.92
z_0^{LOC}	0.05	0.04	0.06	0.08	0.05	0.05	0.04	0.04
z_0^{LVI}	0.13	0.32	0.30	0.33	0.30	0.29	0.30	0.34
z_0^{MTR}	0.08	0.96	0.01	0.02	0.02	0.01	0.95	0.80
z_0^{OCT}	0.92	0.91	0.18	0.52	0.47	0.67	0.16	0.12
z_0^{PDA}	0.04	0.04	0.04	0.04	0.04	0.05	0.02	0.03
z_0^{PST}	0.12	0.07	0.13	0.14	0.13	0.13	0.00	0.14
z_0^{RMB}	0.00	0.00	0.00	0.00	0.00	0.00	0.00	0.00
z_0^{SDN}	0.02	0.02	0.00	0.02	0.03	0.00	0.02	0.03
z_0^{SNE}	0.03	0.02	0.02	0.02	0.02	0.03	0.03	0.03
z_0^{VAP}	0.39	0.05	0.09	0.48	0.49	0.43	0.02	0.01
z_0^{ZAU}	1.22	0.05	0.84	0.95	0.20	0.04	0.05	0.93
z_0^{ZEV}	0.14	0.12	0.12	0.15	0.04	0.14	0.16	0.15
z_0^{ZQM}	0.20	0.74	0.58	0.35	0.47	0.49	0.38	0.76
d^{ACM}	4.80	82.2	77.3	55.9	38.4	75.6	80.8	84.1
d^{ARR}	0.52	0.79	0.72	0.07	0.66	0.64	0.57	0.51
d^{CLC}	0.16	0.13	0.37	0.17	0.07	0.35	0.31	0.17
d^{CNF}	19.7	13.3	6.27	17.5	8.59	10.4	20.4	13.3
d^{CHL}	2.20	0.23	0.48	2.01	2.97	0.55	2.95	1.06
d^{EDF}	10.1	19.1	19.6	10.9	17.4	19.3	7.02	12.8
d^{FDC}	21.4	7.43	10.5	19.4	16.9	6.25	19.8	3.23
d^{FDP}	27.8	3.93	10.7	30.7	18.7	8.10	29.3	4.26
d^{HMA}	0.14	0.54	0.38	0.15	0.76	0.20	0.56	0.42
d^{HSM}	0.06	0.09	0.03	0.10	0.16	0.06	0.04	0.06
d^{LFC}	1.77	0.68	0.32	3.82	2.34	1.25	3.82	0.30
d^{LFN}	1.29	0.50	0.33	1.39	0.60	2.31	2.40	1.58
d^{LOC}	0.34	0.27	0.37	0.23	0.41	0.20	0.34	0.38
d^{LVI}	1.03	0.79	0.76	0.88	0.81	0.75	0.90	1.04
d^{MTR}	2.53	1.07	5.08	6.01	7.06	6.95	6.89	6.84
d^{OCT}	13.9	13.1	6.07	10.3	11.9	13.9	13.4	11.6
d^{PDA}	0.20	0.15	0.12	0.20	0.31	0.19	0.03	0.15
d^{PST}	0.55	0.49	0.13	0.47	0.56	0.40	0.30	0.37
d^{RMB}	0.01	0.02	0.01	0.00	0.02	0.01	0.02	0.00
d^{SDN}	0.09	0.04	0.13	0.06	0.20	0.15	0.04	0.07
d^{SNE}	0.09	0.02	0.09	0.07	0.09	0.05	0.03	0.12
d^{VAP}	2.50	0.32	2.07	2.36	2.47	2.31	0.65	2.08
d^{ZAU}	9.30	5.23	5.81	13.8	13.7	8.64	10.5	10.7
d^{ZEV}	0.17	0.69	0.37	0.70	0.25	0.20	0.73	0.60
d^{ZQM}	3.61	5.40	3.04	3.68	2.10	4.47	2.50	3.14

we can analyze all the wind condition types (speed, direction, stability) occurring in Gran Canaria.

4.4 Conclusions

This chapter presents Wind3D, a mass-consistent diagnostic model with an updated vertical wind profile and atmospheric parameterization which uses an initial wind field with a logarithmic wind profile that consider the effect of both stable boundary layer (SBL) and the convective boundary layer (CBL).

The strategy adopted to deal with the sensitivity of the models to the value of some of its parameters is to estimate their values using a memetic algorithm.

A numerical experiment over Gran Canaria island shows that this model is a suitable tool to study wind fields over complex terrains.

References

1. Abtey, W., Gregory, J.M., Borrelli, J.: Wind profile: Estimation of displacement height and aerodynamic roughness. *Transactions of the ASAE* **32**(2), 0521–0527 (1989). DOI 10.13031/2013.31034
2. Apsley, D.D., Castro, I.P.: Flow and dispersion over hills: comparison between numerical predictions and experimental data. *J Wind Eng Ind Aerod* **67–68**, 375–386 (1997). DOI 10.1016/S0167-6105(97)00087-1
3. Barnard, J.C.: An evaluation of three models designed for siting wind turbines in areas of complex terrain. *Sol Energy* **46**(3), 283–294 (1991). DOI 10.1016/0038-092X(91)90096-F
4. Burlando, M., Georgieva, E., Ratto, C.F.: Parameterisation of the planetary boundary layer for diagnostic wind models. *Bound-Lay Meteorol* **125**, 389–397 (2007). DOI 10.1007/s10546-007-9220-7
5. Byrd, R.H., Lu, P., Nocedal, J., Zhu, C.: A limited memory algorithm for bound constrained optimization. *SIAM J Sci Comput* **16**(5), 1190–1208 (1995). DOI 10.1137/0916069. URL <http://dx.doi.org/10.1137/0916069>
6. Dong, Z., Gao, S., Fryrear, D.W.: Drag coefficients, roughness length and zero-plane displacement height as disturbed by artificial standing vegetation. *J Arid Environ* **49**(3), 485–505 (2001). DOI 10.1006/jare.2001.0807. URL <http://dx.doi.org/10.1006/jare.2001.0807>
7. Ferragut, L., Montenegro, R., Montero, G., Rodríguez, E., Asensio, M.I., Escobar, J.M.: Comparison between 2.5-D and 3-D realistic models for wind field adjustment. *J Wind Eng Ind Aerod* **98**(10–11), 548–558 (2010). DOI 10.1016/j.jweia.2010.04.004
8. Greiner, D., Emperador, J.M., Winter, G.: Single and multiobjective frame optimization by evolutionary algorithms and the auto-adaptive rebirth operator. *Comput Methods Appl Mech Engrg* **193**(33–35), 3711–3743 (2004). DOI 10.1016/j.cma.2004.02.001. URL <http://dx.doi.org/10.1016/j.cma.2004.02.001>
9. Hestenes, M.R., Stiefel, E.: Methods of Conjugate Gradients for Solving Linear Systems. *Journal of Research of the National Bureau of Standards* **49**(6), 409–436 (1952)
10. Homicz, G.F.: Three-dimensional wind field modeling: a review. SAND Report 2597. Tech. rep., Sandia National Laboratories, Albuquerque, NM (2002)
11. Lopes, A.M.G.: Windstation a software for the simulation of atmospheric flows over complex topography. *Environ Model Softl* **18**(1), 81–96 (2003). DOI 10.1016/S1364-8152(02)00024-5

12. Maurizi, A., Palma, J.M.L.M., Castro, F.A.: Numerical simulation of the atmospheric flow in a mountainous region of the north of portugal. *J Wind Eng Ind Aerod* **74–76**, 219–228 (1998). DOI 10.1016/S0167-6105(98)00019-1
13. Mohan, M., Siddiqui, T.A.: Analysis of various schemes for the estimation of atmospheric stability classification. *Atmos Environ* **32**(21), 3775–3781 (1998). DOI 10.1016/s1352-2310(98)00109-5. URL [http://dx.doi.org/10.1016/s1352-2310\(98\)00109-5](http://dx.doi.org/10.1016/s1352-2310(98)00109-5)
14. Montavon, C.: Validation of a non-hydrostatic numerical model to simulate stratified wind fields over complex topography. *J Wind Eng Ind Aerod* **74–76**, 273–282 (1998)
15. Montero, G., Montenegro, R., Escobar, J., Rodríguez, E.: Resolution of sparse linear systems of equations: the rpk strategy. In: B. Topping, C.M. Soares (eds.) *Progress in Engineering Computational Technology*, chap. 5, pp. 81–109. Saxe-Coburg Publications, Stirlingshire, UK (2004)
16. Montero, G., Montenegro, R., Escobar, J.M.: A 3-D diagnostic model for wind field adjustment. *J Wind Eng Ind Aerod* **74–76**, 249–261 (1998). DOI 10.1016/S0167-6105(98)00022-1
17. Montero, G., Rodríguez, E., Montenegro, R., Escobar, J., González-Yuste, J.: Genetic algorithms for an improved parameter estimation with local refinement of tetrahedral meshes in a wind model. *Advances in Engineering Software* **36**(1), 3 – 10 (2005). DOI <https://doi.org/10.1016/j.advengsoft.2004.03.011>. URL <http://www.sciencedirect.com/science/article/pii/S0965997804000742>. Evolutionary Optimization of Engineering Problems
18. Montero, G., Rodríguez, E., Montenegro, R., Escobar, J.M., González-Yuste, J.M.: Genetic algorithms for an improved parameter estimation with local refinement of tetrahedral meshes in a wind model. *Adv Eng Softw* **36**(1), 3–10 (2005). DOI 10.1016/j.advengsoft.2004.03.011
19. Mortensen, N.G., Landberg, L., Troen, I., Petersen, E.L.: *Wind atlas analysis and application program (WAsP)*. Vol. 2: Users guide. Riso National Laboratory, Roskilde, Denmark (1993)
20. Oliver, A., Rodríguez, E., Escobar, J.M., Montero, G., Hortal, M., Calvo, J., Cascón, J.M., Montenegro, R.: Wind forecasting based on the harmonie model and adaptive finite elements. *Pure and Applied Geophysics* **172**(1), 109–120 (2015). DOI 10.1007/s00024-014-0913-9. URL <https://doi.org/10.1007/s00024-014-0913-9>
21. Sherman, C.A.: A mass-consistent wind model for wind fields over complex terrain. *J Appl Meteorol* **17**(3), 312–319 (1978)
22. Storn, R., Price, K.: Differential Evolution – A Simple and Efficient Heuristic for Global Optimization over Continuous Spaces. *J Global Optim* **11**(4), 341–359 (1997). DOI 10.1023/a:1008202821328. URL <http://dx.doi.org/10.1023/a:1008202821328>
23. Suárez, A., Sarmiento, H., Flórez, E., García, M., Montero, G.: Updating incomplete factorization preconditioners for shifted linear systems arising in a wind model. *Journal of Computational and Applied Mathematics* **235**(8), 2640–2646 (2011). DOI <https://doi.org/10.1016/j.cam.2010.11.015>. URL <http://www.sciencedirect.com/science/article/pii/S0377042710006321>
24. Uchida, T., Ohya, Y.: Numerical simulation of atmospheric flow over complex terrain. *J Wind Eng Ind Aerod* **81**(1–3), 283–293 (1999). DOI 10.1016/S0167-6105(99)00024-0
25. Wagenbrenner, N.S., Forthofer, J.M., Lamb, B.K., Shannon, K.S., Butler, B.W.: Downscaling surface wind predictions from numerical weather prediction models in complex terrain with windninja. *Atmos Chem Phys* **16**(8), 5229–5241 (2016). DOI 10.5194/acp-16-5229-2016. URL www.atmos-chem-phys.net/16/5229/2016/
26. Walmsley, J.L., Taylor, P.A., Keith, T.: A simple model of neutrally stratified boundary layer flow over complex terrain with surface roughness modulations (ms3djh/3r). *Bound-Lay Meteorol* **36**(1–2), 157–186 (1986). DOI 10.1007/BF00117466
27. Walmsley, J.L., Troen, I.B., Demetrius, P., Lalas, D.P., Mason, P.J.: Surface-layer flow in complex terrain: comparison of models and full-scale observations. *Bound-Lay Meteorol* **52**(3), 259–281 (1990). DOI 10.1007/BF00122090
28. Winter, G., Montero, G., Ferragut, L., Montenegro, R.: Adaptive strategies using standard and mixed finite elements for wind field adjustment. *Solar Energy* **54**(1), 49 – 56 (1995). DOI [https://doi.org/10.1016/0038-092X\(94\)00100-R](https://doi.org/10.1016/0038-092X(94)00100-R). URL <http://www.sciencedirect.com/science/article/pii/S0038092X9400100R>

29. Zilitinkevich, S.S., Fedorovich, E.E., Shabalova, M.V.: Numerical model of a non-steady atmospheric planetary boundary layer, based on similarity theory. *Bound-Lay Meteorol* **59**, 387–411 (1992)
30. Zilitinkevich, S.S., Johansson, P.E., Mironov, D.V., Baklanov, A.: A similarity-theory model for wind profile and resistance law in stably stratified planetary boundary layers. *J Wind Eng Ind Aerod* **74–76**, 209–218 (1998)
31. Zilitinkevich, S.S., Tyuryakov, S.A., Troitskaya, Y.I., Mareev, E.A.: Theoretical models of the height of the atmospheric boundary layer and turbulent entrainment at its upper boundary. *Atmospheric and Oceanic Physics* **48**(1), 150–160 (2012). DOI 10.1134/S0001433812010148

